



Calendar Aging and Gas Generation in Commercial Graphite/NMC-LMO Lithium-Ion Pouch Cell

Z. Mao, M. Farkhondeh,* M. Pritzker,*^z M. Fowler, and Z. Chen*

Department of Chemical Engineering, University of Waterloo, Waterloo, Ontario N2L 3G1, Canada

The calendar life of a commercial graphite/NMC-LMO lithium-ion battery is assessed under various storage temperature (35°C and 60°C) and state-of-charge (0% and 100%) conditions. Virtually no degradation is observed for cells stored at 0% SOC as expected, whereas those aged for 9 months in a fully charged state at 35°C and 60°C lose ~10% and ~43% of their capacity, respectively. Differential-voltage analysis of periodic cell cycling data and post-mortem examination of the aged electrodes are used to identify degradation modes. Three main sources of high-temperature capacity loss are identified: i) electrode dry-out due to gas formation (~30%), ii) loss of cyclable lithium (~10%) and iii) cathode active material loss (~3%). Cells stored at a lower temperature of 35°C experience little gas generation and degrade primarily through the loss of Li inventory. The analysis shows that similar amounts of cyclable Li are consumed by side reactions during calendar aging at both storage temperatures of 35°C and 60°C. Non-destructive compression (1.0–5.0 psi) of the aged pouch cells during discharge is shown to improve their capacity by ~15%. This effect is attributed to the redistribution of gas bubbles inside the pouch cell by the applied pressure.

© The Author(s) 2017. Published by ECS. This is an open access article distributed under the terms of the Creative Commons Attribution 4.0 License (CC BY, <http://creativecommons.org/licenses/by/4.0/>), which permits unrestricted reuse of the work in any medium, provided the original work is properly cited. [DOI: 10.1149/2.0241714jes] All rights reserved.



Manuscript submitted September 12, 2017; revised manuscript received October 30, 2017. Published November 11, 2017.

After undergoing several generations of development as energy storage devices, lithium-ion batteries (LIBs) are now widely used in consumer electronic products and their designs are being broadened for use in the automotive industry. The introduction of commercial LIBs consisting of $\text{LiNi}_x\text{Mn}_y\text{Co}_{1-x-y}\text{O}_2$ - LiMn_2O_4 (NMC-LMO) blended cathodes and graphite anodes has been so successful that they now dominate the burgeoning market of automotive LIBs due to their superior performance and lower price compared to conventional LiCoO_2 cathodes.¹ In order to continue optimizing the design of these batteries, a number of experimental and modeling studies on the operating behavior, life cycle, degradation mechanism, etc., of blended cathodes have been conducted. Jung² developed a mathematical model for a graphite-soft carbon/NMC-LMO cell for the purpose of designing new electrodes and predicting the performance of the cell with different cathode compositions. In our previous studies,^{3,4} we developed a model-based approach to identify the composition of an unknown blended cathode and presented a multi-particle model to describe the electrochemical performance at different charge/discharge rates that accounts for the effects of particle size distribution and solid-state diffusivities in a commercial NMC-LMO (70:30 wt%) cathode. The model also was used to explain the asymmetry between charge and discharge behavior of the blended electrode⁵ and describe its internal dynamics during intermittent operation.⁶

Several research groups have studied the cycling^{7–10} and calendar aging^{11,12} of commercial cylindrical graphite/NMC-LMO batteries and identified the loss of capacity due primarily to SEI growth and secondarily to the loss of active materials (e.g., active particle breakage, isolation and transition metal dissolution). Moreover, these processes were shown to be strongly affected by the discharge/charge rate and temperature in the case of cycle aging and by temperature, state-of-charge (SOC) or storage voltage in the case of calendar aging. Using ultrahigh-precision coulometry, Stevens et al.¹³ investigated degradation mechanisms in a graphite/NMC-LMO pouch cell at temperatures between 25°C and 50°C and showed that the loss of cyclable lithium due to SEI growth on the anode was the main contributor to the overall capacity fade of the cell although evidence of a small amount of electrolyte oxidation on the cathode was also found.

In addition to the loss of cyclable lithium, SEI growth and the rise in cell impedance, parasitic reactions in both positive and negative electrodes lead to the generation of gaseous species which inflates the pouch cell and also contributes to battery degradation. Electrolyte additives are commonly used to decrease gas formation and improve

the quality of the passivating film on the surface of active particles.¹⁴ These parasitic reactions involve the electrolyte components (solute, solvent, additives and trace impurities) as well as the solid, liquid and gaseous by-products themselves which make these reactions difficult to identify, characterize and model. The formation cycles (i.e., first few charge/discharge cycles after the cell is manufactured to form SEI on the negative electrode particles) should ideally stabilize the electrodes and diminish their reactivity with the electrolyte by producing perfectly passive layers on the active particle surfaces. Of course, the passivating layers are never perfect; pores and cracks in the SEI layer (i.e., leakage of side reaction reagents to the surface of the active material) and/or the catalytic effect of deposited transition metals originating from the positive electrode promote continuous electrolyte decomposition, although at a much lower rate compared to that during the formation cycles.

Gas generation in cells has been reported to occur primarily during the formation cycles. In a series of publications, Dahn and co-workers used gas chromatography (GC-MS and GC-TCD) and a lab-made apparatus based on Archimedes' principle to investigate gas generation during the formation cycles of batteries filled with various electrolyte formulations.^{14–20} The gaseous species were shown to be mostly generated at the onset of the first charging step (i.e., low voltages) and then almost entirely consumed throughout the remainder of the formation period.¹⁴ This low voltage generation of gases such as C_2H_4 , C_2H_6 and CO_2 is presumably associated with the reduction of the electrolyte solvent on the negative electrode, while their consumption involves their subsequent reduction to oxalate or polymeric species. Gas formation (e.g., CO_2) was also observed when cells were charged to high enough voltages (above 4.2 V) presumably due to electrolyte solvent oxidation on the positive side. Some of this gas is then consumed by reduction on the negative electrode (e.g., reduction of CO_2 to oxalate).^{15,17} It has been shown that for given electrolyte, additives and electrode pairs, an increase in temperature causes gas evolution to occur at lower voltages and the total amount of gas generated to increase significantly.

Xia et al.¹⁶ investigated formation, cycling and storage of graphite/NMC pouch cells (cells balanced for a 2.8–4.2 V voltage window) with different electrolyte additives and observed that the volume of gas generated during the formation cycles (up to ~13 mL Ah^{-1}) was roughly correlated to the amount of irreversible capacity loss. This implied that the additives affected the amount of irreversible capacity loss and gas formation similarly. The same trend was observed during the subsequent storage (up to ~2.7 mL Ah^{-1} for 500 h storage at 40°C and 100% SOC). However, the subsequent cycling test showed deviations from this trend; for instance, cells which had generated a larger amount of gas during formation and

*Electrochemical Society Member.

^zE-mail: pritzker@uwaterloo.ca

storage consumed a larger portion of these gaseous species during subsequent charge/discharge cycles (up to ~ 0.6 mL Ah⁻¹ in about 350 cycles at 1C and 40°C). Belharouak et al.²² observed significant generation of gases (primarily H₂, CO₂, CO, CH₄ and C₂H₆) in LTO/LMO pouch cells during storage at a fully charged state at 3 V. Furthermore, the amount of gas generated increased in cells stored at higher temperatures. It was hypothesized that H₂ is generated as a result of water splitting during storage. Broussely et al.²² showed that electrolyte oxidation at the positive electrode leading to CO₂ evolution becomes significant over long storage periods for LiCoO₂-based and LiNi_xCo_yAl_zO₂-based cells at elevated temperatures and high SOC. The cell pressure evolved differently in LiNi_xCo_yAl_zO₂-based and LiCoO₂-based cells, indicating that electrolyte oxidation depends strongly on the nature of the cathode material and its impurities (e.g., Li₂CO₃).

Using the so-called pouch bag method, Xiong et al.^{19,20,23} studied gas generation in graphite/NMC111 pouch cells, graphite/NMC442 pouch cells and air-tight pouch bags that contain either the positive electrode or the negative electrode flooded with fresh electrolyte. These pouch bags were used to investigate the interactions between the electrolyte and each of the positive and negative electrodes in the absence of the other electrode. The graphite and NMC electrodes were harvested from the pouch cells that had undergone certain formation protocols to assure proper SEI formation and that the lithiation states of the NMC and graphite electrodes stored in the pouch bags were identical to those in the pouch cells. The pouch cells and pouch bags were stored at 40°C and 60°C for 500 hours. It was observed that delithiated cathodes in the electrolyte-filled bags produced more gas (mostly CO₂) than those in pouch cells while virtually no gas was generated in the graphite pouch bags, similar to that reported in earlier studies on pouch bags containing lithiated graphite and delithiated LiCoO₂ (LCO) and Li[Ni_{0.80}Co_{0.15}Al_{0.05}]O₂ (NCA).²⁴ CO₂ intentionally injected into the electrolyte-filled lithiated graphite bags was consumed, confirming that it can be consumed at the negative electrode (likely via reduction) in an actual pouch cell during normal operation after being produced at the positive electrode due to electrolyte solvent oxidation at high enough voltages. Also, hydrogen was found in pouch cells, but not pouch bags, suggesting that both electrodes in the cell are required for its appearance.²⁰ Considering the detrimental effect of gas formation on battery life, Michalak et al.²⁵ suggests that proper cell formation procedure is necessary to improve battery durability.

Poor thermal stability of carbonate-based electrolytes is another source of degradation of Li-ion batteries at elevated temperatures. Reaction of the unstable SEI on the anode particles with electrolyte at high temperatures consumes the SEI and increases the rate of electrolyte solvent reduction. The formation of a passivating film on the cathode particles is also sensitive to temperature. As well, the bulk electrolyte itself is prone to chemical decomposition at elevated temperatures. Campion et al.²⁶ investigated the thermal decomposition of solutions of LiPF₆ in carbonate-based solvents and observed the formation of solid, liquid and gaseous species (e.g., CO₂, C₂H₄) after the solution was stored at elevated temperatures (85–100°C) for one to four weeks. Trace protic contaminants (e.g., H₂O and C₂H₅OH) were found to accelerate autocatalytic electrolyte decomposition.

In this work, we investigate the effect of storage at various temperature and SOC conditions on the calendar life of commercial 15 Ah pouch cells containing graphite/NMC-LMO active materials. The experiments conducted involve periodic characterization tests and simple post-mortem analysis in order to gain more insight into the mechanisms for capacity fade. It is found that the loss of cyclable Li inventory due to SEI growth and gas formation are the main sources of capacity degradation in the commercial pouch cells studied. The loss of Li inventory and effect of gas formation on the cell capacity fade are quantified using differential-voltage analysis (DVA) of periodic galvanostatic charge data. It turns out that gas formation in the commercial cells investigated can cause significant capacity loss even after a relatively short storage period. Finally, the non-destructive loading of pressures on the pouch cells during charge and discharge is carried out and found to dramatically improve the achievable capacity

of the aged cell even at very low pressures. The loading of pressure helps redistribute the gas generated by the side reactions and tighten the connection between cell components leading to faster ionic (and possibly electronic) transfer and better utilization of the active materials during charge and discharge. This pressure loading approach is a relatively simple and effective method to ensure a high-performance life of pouch cells designed particularly for electric and hybrid electric vehicles applications. This suggests an additional criterion for the design of pouch cell modules whereby the internal pressure is optimized not only for thermal management but also for extended battery life.

Experimental

Calendar-life experiments.—The calendar life study was conducted on eight commercial Li-ion pouch cells comprised of an NMC-LMO blended cathode (7:3 mass ratio of NMC:LMO) and a graphite anode with a nominal capacity of 15 Ah for application in plug-in hybrid electric vehicles (PHEVs). Each commercial pouch cell consisted of 16 double-side-coated rectangular positive sheets (18.9 cm × 14.15 cm) and 17 negative sheets (19.2 cm × 14.5 cm). Two cells were stored under each of the following four conditions: 0% SOC at 35°C, 0% SOC at 60°C, 100% SOC at 35°C and 100% SOC at 60°C. In this way, duplicate experiments were conducted for each condition. This allowed us to determine the variability in the cell capacity and voltage data obtained from the two replicate pouch cells.

Prior to storage, each fresh as-received pouch cell (initially at 50% SOC) was characterized in terms of its capacity and rate capability and then discharged to 0% or charged to 100% SOC using a battery cycler (MACCOR model 4200, USA). The capacity and rate capability of each cell were determined by subjecting it to constant-current-constant-voltage (CC-CV) charge/discharge cycles consisting of the following steps: i) discharge at a specified C-rate until a voltage of 2.8 V was reached, ii) discharge at a constant voltage of 2.8 V until a current of C/20 was reached, iii) 10-min rest, iv) charge at the same C-rate until a voltage of 4.15 V was reached, v) charge at a constant voltage of 4.15 V until a current of C/20 was reached and vi) 10-min rest. The rate capabilities of the cells at various C-rates were determined by applying CC-CV cycles at currents of C/5, C/2, 1C and 2C. The cells underwent a sequence of three CC-CV conditioning cycles at 1C prior to the rate capability test. The upper cutoff voltage of 4.15 V and the lower cutoff voltage of 2.8 V were chosen based on information provided by the manufacturer. The battery is assumed to be fully charged (i.e., 100% SOC) at 4.15 V and fully discharged (i.e., 0% SOC) at 2.8 V.

Two of the 0% SOC cells and two of the 100% SOC cells were placed in a temperature-controlled chamber operating at 35°C, while the other four cells were placed in a chamber at 60°C. These cells were stored at open-circuit in both temperature-controlled chambers. In order to monitor the change in the performance of these cells upon aging, they were characterized at 1-month intervals according to the following procedure. The cells were removed from the chambers and then allowed to cool to room temperature and stabilize for at least 4 hours prior to performing 1C cycling and rate capability tests. The capacities were recorded at the end of a C/5 CC-CV charge and discharge cycle. After completion of the 1C cycling and rate capability tests, the cells were restored back to their assigned SOC (0% or 100%) and placed back in the temperature-controlled chambers. Since the battery capacity degraded during aging, we set the 0% and 100% SOC to be the states at which the cell voltages reached the lower (2.8 V) and upper (4.15 V) cutoff voltages, respectively, and could maintain this level until the current reached C/20. The C-rates were referred to the nominal cell capacity of 15 Ah.

Post-mortem experiments.—Half-cell electrochemical experiments were conducted on the positive and negative electrodes taken from one of the pouch cells after 9 months of storage at 100% SOC and 60°C. The second pouch cell stored under this condition was aged for 12 months before undergoing compression tests as described later. Only one aged cell was dismantled for post-mortem experiments. For

comparison, similar half-cell tests were done on electrodes obtained from fresh, unused pouch cells. Care was taken to ensure that the pouch cells were fully discharged before being disassembled. Cathode and anode sheets were removed from the middle portions of fresh and aged cells and then the coating on one side of these electrode sheets was dissolved away using N-methyl-2-pyrrolidone (NMP) solvent. Circular samples (0.712 cm^2) were then punched from these sheets coated on one side so that they could be assembled into coin cells. In order to remove any electrolyte salt that had possibly been deposited, the circular samples were rinsed in dimethyl carbonate (DMC) several times. The coin cells consisted of a working electrode (washed circular samples of either the positive or negative electrodes) and a Li foil reference/counter electrode separated by a Celgard 2500 separator. The electrodes and separator were soaked in a 1 M LiPF₆ in 1:1 EC/DMC solution as electrolyte. The same procedure was used to fabricate the coin cells from fresh and aged positive and negative sheets. In order to assess the repeatability of our measurements, we made two coin cells from positive electrode removed from each pouch cell and two coin cells from the negative electrode taken from the same pouch cell. The two coin cells in each case were fabricated from samples taken from different sheets of the same pouch cell – one was located in the middle of the pouch cell, while the other was close to the cell casing. The data obtained from the samples at these two locations within each pouch cell were found to be very similar in all of the samples examined, indicating that the sheet-to-sheet variability within each pouch cell was small. The entire process of disassembling the pouch cells and fabricating the coin cells was conducted in an argon-filled glove box (H_2O , O_2 concentrations $\ll 1$ ppm).

A series of galvanostatic experiments was carried out on both the anode and cathode half-cell coin cells using a coin cell tester (Neware CT-3008-5 V 10mA-164-U, China). Prior to these experiments, each cell was subjected to five formation cycles conducted at a current of 1 mA ($\sim 0.69\text{C}$ for the cathode half-cells and $\sim 0.60\text{C}$ for the anode half-cells), as described in our previous studies,^{3,4} to ensure that it had attained a stable electrochemical state. The specific galvanostatic experiments for the cathode half-cells consisted of rate capability tests conducted in the sequence C/10, C/5, C/2, 1C and 2C over the potential window from 3.0 V to 4.2 V and C/25 galvanostatic charge/discharge over the potential window from 3.0 V to 4.4 V. 1C corresponded to 1.44 mA applied current in the case of the cathode half-cells. A similar testing profile was used for the anode half-cells. The upper and lower cutoff potentials were 1.5 V and 0.005 V, respectively, for all anode rate capability experiments. 1C was equivalent to an applied current of 1.66 mA in the anode half-cells.

To characterize the degradation of the positive electrodes, we used ICP-OES analysis (ProdigyPlus, Teledyne Leeman Labs, USA) to measure the amount of transition metals (Mn, Ni and Co) present in the negative electrode harvested from a fresh cell and one of the cells aged for 9 months at 60°C and 100% SOC storage condition. The procedure followed to prepare samples for the ICP-OES analysis involved washing the electrode layer with DMC, scraping the electrode off the current collector and then digesting it in 20% HCl/HNO₃ solution (1:1) for 6 hours at 90°C , which was long enough to dissolve the SEI layer but not the graphite particles themselves. Elemental analysis was also carried out using an Oxford EDS system (AZtec) equipped on a Zeiss LEO field emission scanning electron microscope.

Pressure loading experiments.—We used a custom-made compression set-up to investigate the effect of loading small pressures on the pouch cells during their galvanostatic cycling. As shown in Figure 1, it consisted of a metal-only copper-tin plate on top of two copper-tin-plastic sheet assemblies each of which consisted of a plastic sheet ($23.5 \text{ cm} \times 24 \text{ cm}$) glued to a copper-tin plate. The top plate was separated from the upper copper-tin-plastic plate by four springs. The copper-tin-plastic plates were oriented so that the two plastic sheets faced each other in the middle. A pouch cell was tested by placing it between the plastic sheets of the copper-tin-plastic assemblies and applying pressure to this stack using an ADMET instrument (model SM-1000-38, USA). The screws mounted on top of the four springs

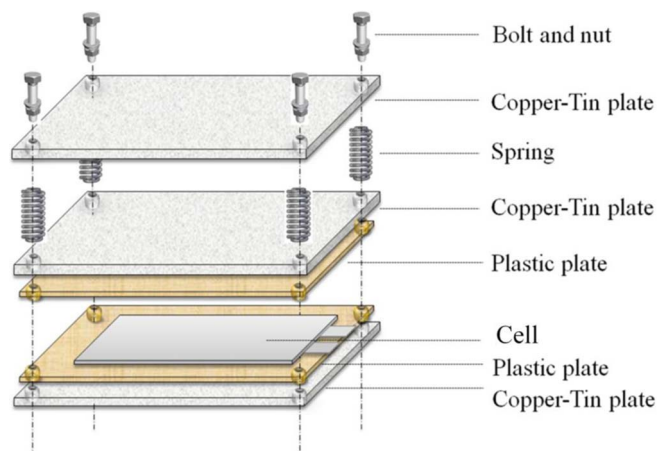


Figure 1. Cell compression set-up.

were then tightened to maintain the adjusted pressure before the compression fixture was removed from the pressure loading instrument and connected to the battery cycler.

This set-up was used to study the effect of external pressure on the performance of cells stored and aged in a fully charged state at 60°C . In the first experiment, the cell was charged and discharged at the rate of C/25 while being subjected to a pressure of 4.0 psi ($\sim 763 \text{ N}$). Then, the pressure on the pouch cell was adjusted in steps following the order shown in Figure 2 and the corresponding voltage-capacity data at C/25 were obtained at the end of each step.

Results and Discussion

Capacity degradation.—The variation in the capacity of the pouch cells during the course of the four aging experiments as measured at the end of discharges at the rates of C/5, C/2, 1C and 2C as well as the CC-CV capacities (CV discharge step finished when the current reached C/20) is presented in Figure 3. Interestingly, the CC-CV capacities of the cells that are stored at 0% SOC slightly increase during the early stages of aging before slightly decreasing thereafter (Figures 3a and 3b). The CC-CV capacities of the cells stored at 35°C and 0% SOC remain above their initial capacities even after 10 months of aging. For cells stored at 60°C and 0% SOC, the achievable CC-CV capacities are very close to their initial level even after 10 months of aging. This initial rise in capacity has been reported previously.^{27–29} Lewerenz et al.²⁹ proposed the so-called “passive electrode effect” to

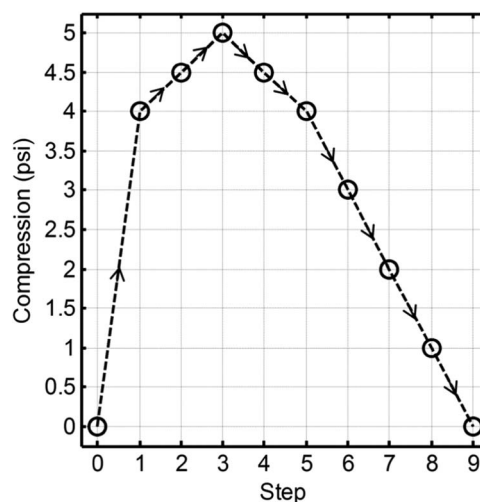


Figure 2. Pressure-path profile for testing cell capacity.

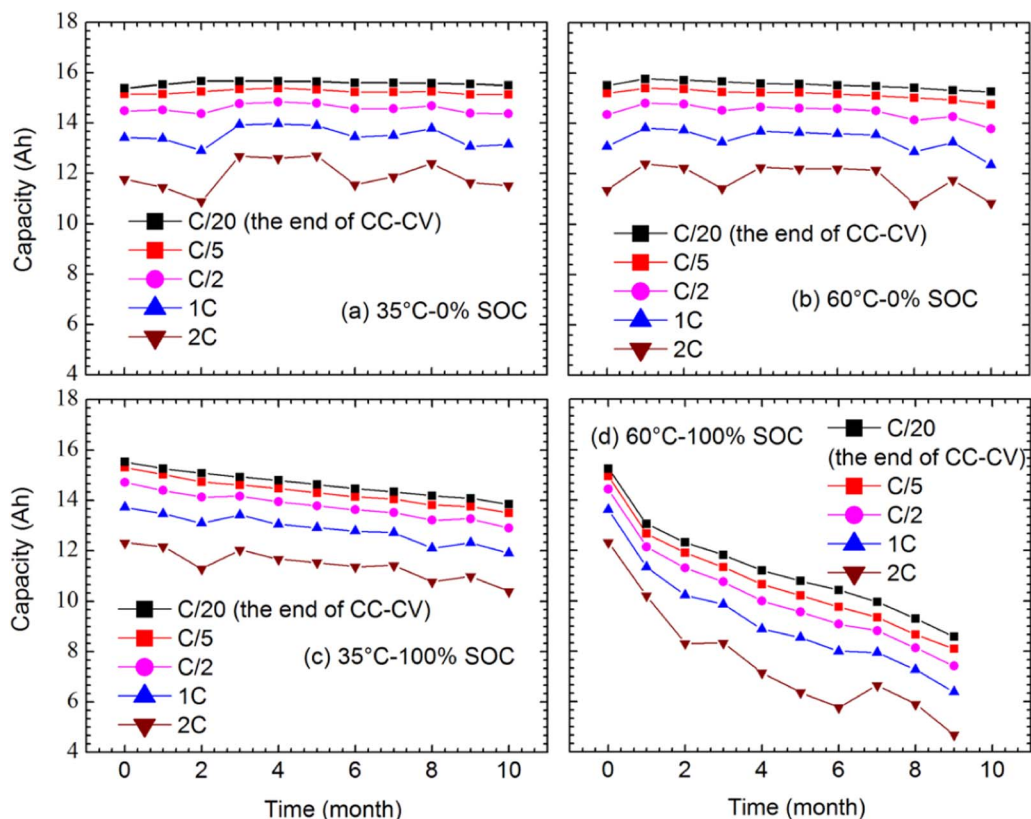


Figure 3. Effect of storage temperature and SOC on the degradation of pouch cell capacities measured at discharge rates of C/5, C/2, 1C and 2C and the end of CC-CV discharge: (a) 35°C, 0% SOC (b) 60°C, 0% SOC (c) 35°C, 100% SOC and (d) 60°C, 100% SOC.

explain the capacity rise of commercial $\text{LiFePO}_4/\text{graphite}$ cylindrical cells during calendar aging. In commercial cells, excess graphite capacity is usually available in the electrode overhang (i.e., oversized negative electrode sheets compared to the positive sheets) at the edge of the negative electrode. The rise in capacity occurs as a result of the compensating flow of cyclable lithium within the negative electrode between this “passive” part and the active area. Anomalous fluctuations in the cell capacities visible at high rates (1C and 2C) are experimental artifacts and related to the variations in the room temperature ($\pm 2^\circ\text{C}$) during the periodic test intervals.

The pouch cells stored at 100% SOC age very differently than those stored at 0% SOC (Figures 3c and 3d). Not only does the capacity continually drop as the duration of storage lengthens but also the capacity loss is severe and storage temperature is found to have a much larger effect in cells stored at 100% SOC compared to those aged at 0% SOC. Figure 4 compares the capacity decay of cells aged at 35°C and 60°C under 100% SOC. After 9 months, the cell retains ~90% of its initial capacity when stored at 35°C, while only ~57% of the capacity remains in the cells stored at 60°C after the same period of storage time. The capacity of the cells stored at 100% SOC and 60°C always degrade most rapidly, whereas those stored at 0% SOC and 35°C degrade most slowly. At 60°C and 100% SOC, bulges appear in the pouch cells during storage, revealing that a considerable amount of gas is being generated.

Reversible capacity loss of the cells stored at 100% SOC and the effect of periodic cycling tests on capacity degradation are investigated by plotting CC-CV capacities at the end of the first, second and last periodic discharges presented in Figure 5. From the data shown in Figure 5a, it can be concluded that the intermediate cycling does not have a direct impact on cell degradation since virtually no loss is observed between the second and last cycles. The reversible capacity loss refers to a temporary reduction in discharge capacity during storage which is recovered upon a full charge and discharge cycle.

It is calculated from the difference between the first and second CC-CV intermediate discharge capacities and found to be in the range of ~0.08–0.26 Ah for cells stored at 35°C and ~0.16–0.4 Ah for those stored at 60°C (Figure 5b). Any set of parasitic reactions that

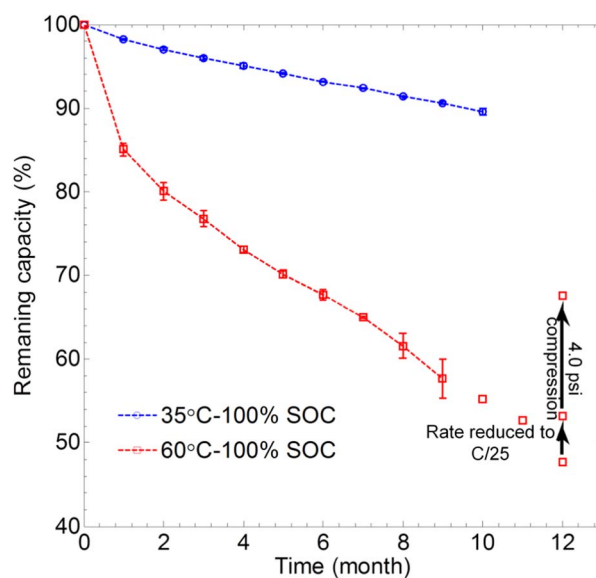


Figure 4. Capacity decay of pouch cells measured at the end of C/5 constant-current discharge during different stages of aging. The impacts of C-rate and cell compression on achievable capacity after 12 months are indicated by the black arrows in the graph. Error bars are determined from the standard deviation in the results of the two replicates.

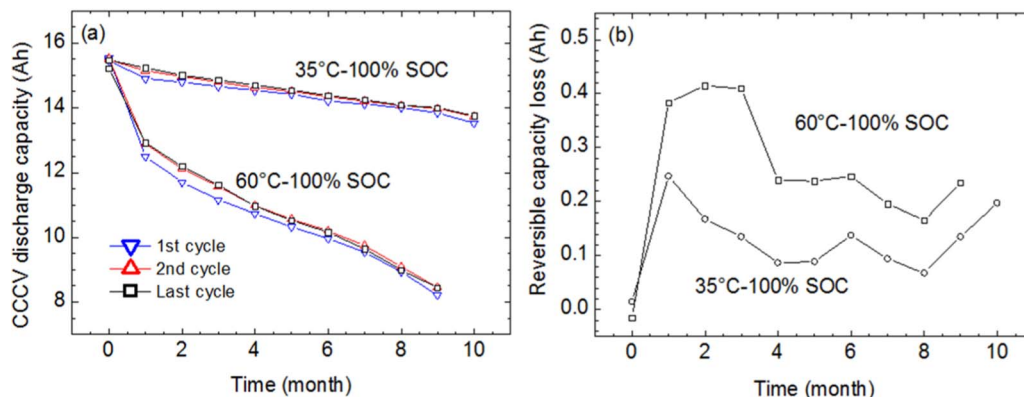


Figure 5. (a) Constant-current constant-voltage capacity at the end of the first, second and last discharge steps during periodic battery testing for cells stored at 100% SOC. (b) The reversible capacity loss of the cells estimated by subtracting the CC-CV capacity at end of the first discharge from that at end of the second one for cells stored at 100% SOC.

transfer Li^+ ions from the graphite particles in the negative electrode to the positive electrode active material leads to a temporary loss of discharge capacity. These side reactions include, but are not limited to a) Li^+ withdrawal from the negative electrode active material due to electrolyte reduction, reduction of a so-called “shuttle” species and transition metal deposition on the negative electrode and b) Li^+ insertion into the positive electrode active material due to electrolyte or shuttle species oxidation and transition metal dissolution.³⁰ The side reactions a) above contribute to the total capacity loss (i.e., reversible + irreversible) of the cell, whereas the losses due parasitic reactions b) are reversible.³¹ In most cases, Li-consuming parasitic reactions on the negative electrode outpace Li-generating side reactions on the positive electrode. Consequently, the larger amount of reversible capacity at the beginning of calendar aging evident in Figure 5b may be attributed to the deceleration of the side reactions occurring at the positive electrode after a few months of cell storage due, for instance, to the development of a passivation layer on the surface of the positive electrode particles.

The voltage-capacity curves obtained from the rate capability experiments before and after 9 months of storage at 100% SOC at 35°C and at 100% SOC at 60°C are compared in Figure 6. These data show that the cells reach only ~89% and ~53% of their initial capacities after aging at 35°C and 60°C, respectively, when the lower cutoff voltage is reached almost independently of the C-rate (Figures 6b and 6e). On the other hand, the capacity attained by the end of charge at the upper cutoff voltage of 4.15 V depends more strongly on the C-rate (Figures 6a and 6d). It decreases considerably as the C-rate is increased from C/5 to 2C; the cells stored at 60°C and 35°C retain ~52% and 89% of their initial capacities, respectively, when charged at C/5 and as low as ~37% and ~66% when charged at 2C.

Post-mortem analysis.—In order to investigate the mechanisms of the observed capacity loss during calendar aging, the fresh cell and the cell aged for 9 months of storage at 100% SOC and 60°C were disassembled and four types of electrode/separator/Li coin cells, i.e., fresh and aged cathodes and anodes, were fabricated as described in the Experimental section. A comparison of the charge/discharge potential-capacity curves and end-of-charge/discharge capacities of the cathode and anode half-cells measured at the rates of C/10, C/5, C/2, 1C and 2C are shown in Figure 7. Figures 7a–7c show that aging leads to a small decrease in the capacity (~2.7% compared to capacity of the fresh electrode) and some increase in the potential loss of the cathode at any given depth of lithiation/delithiation at all currents. The asymmetry in the charge and discharge curves is slightly greater for the aged cathode compared to the fresh one. As shown in our previous study,⁵ the cathode is comprised of a 7:3 (wt%) blend of NMC and LMO active materials. In order to determine whether these capacity losses can be traced to the active materials in the blended elec-

trode, we have obtained the normalized differential-capacity curves (i.e., normalized with respect to C/10 discharge capacity) from the galvanostatic discharge data to examine the effect of aging on the intensities of the signature peaks for NMC (~3.75 V) and LMO (~4.00 V and ~4.14 V). Figure 8 compares the differential-capacity curves of the fresh and aged cathodes over the range of currents from C/10 to 2C. For both the fresh and aged cathodes, the intensity of the NMC peak decreases as the C-rate increases. This is expected because Li diffusion in NMC is the controlling factor at the end of discharge.⁵ The differential-capacity curve of the aged cathode overlaps almost

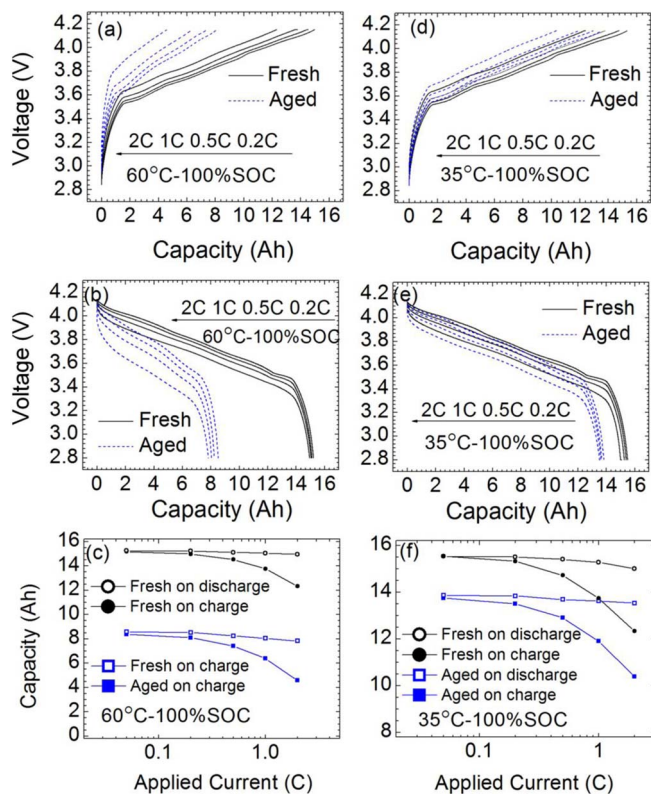


Figure 6. Comparison of voltage-capacity curves obtained from (a) charge and (b) discharge of the fresh cell and cell stored at 60°C and 100% SOC for 9 months and (d) charge and (e) discharge of the fresh cell and cell stored at 35°C and 100% SOC for 9 months. (c), (f) Comparison of capacities at the end of charge and discharge for the fresh cell and cells stored at 60°C and 35°C, respectively.

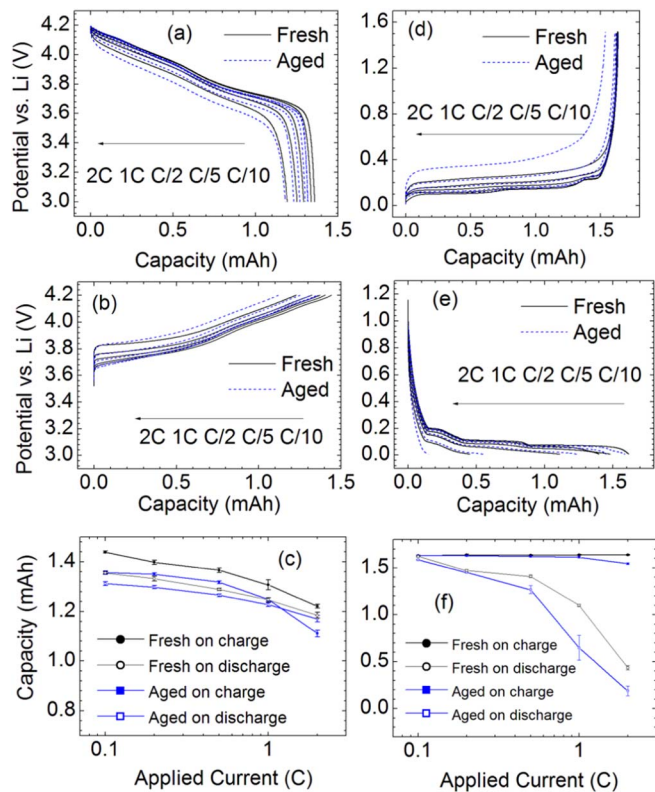


Figure 7. Comparison of potential-capacity curves for (a), (e) lithiation and (b), (d) delithiation of (a), (b) fresh cathode and (d), (e) fresh anode with those removed from the pouch cell aged for 9 months at 100% SOC and 60°C storage condition. End-of-charge/discharge capacity curves of fresh electrodes and those obtained from the cell aged for 9 months at 60°C and 100% SOC are compared in (c) for cathode and (f) for anode. Error bars in (c) and (f) are determined from the standard deviation of the mean values.

perfectly with that of the fresh one at the lowest C-rate, confirming that the capacity losses in both NMC and LMO are small. However, as the discharge current is raised, the peak positions of the aged sample, in particular, shift toward lower potentials and diverge more and more from those of the fresh cathode. Moreover, the NMC/LMO peak intensity ratio is greater for the aged electrode compared to the fresh one, especially at high rates, which may be indicative of a larger increase in the surface resistance of LMO compared to NMC particles due to aging. This is in line with the increased charge/discharge asymmetry and consistent with the trends shown in the potential-capacity curves (Figures 7a and 7b) as the electrode ages.

A comparison of the potential-capacity and of end-of-charge/discharge capacity curves of the fresh and aged anodes is presented in Figures 7d–7f. In addition to the larger potential loss of the aged anode at a given applied current over the entire capacity range compared to the fresh anode at the same current (Figures 7d and 7e), a relatively small loss in capacity is observed ($\sim 0.4\%$) in the electrode at low rates (i.e., up to C/2) although it tends to grow at higher C-rates (Figure 7f). The data presented in Figures 7c and 7f suggest that the decrease in the pouch cell end-of-charge capacity with charge rate (Figures 6c and 6f) is caused primarily by the drop of the achievable lithiation capacity of the negative electrode as the applied current is increased.

The loss of the pouch cell capacity is much larger than that of the coin cells fabricated from its positive and negative electrodes. For example, capacity fades of only $\sim 2.7\%$ and $\sim 0.4\%$ are measured for the cathode and anode, respectively, whereas a $\sim 43\%$ loss is observed for the pouch cell stored at 100% SOC and 60°C from which the coin cells are fabricated (Figure 4). This huge difference indicates that most of the capacity loss of the pouch cell during calendar aging originates from factors that operate in the pouch cell but not in the anode and cathode half-cell coin cells. In a half-cell coin cell, the Li foil counter/reference electrode acts as an infinite source of Li^+ ions whereas the Li^+ ion inventory in a pouch cell is limited by the total capacity of the cathode. Moreover, a coin cell is mechanically more robust than a pouch cell. Thus, one possible cause of the capacity

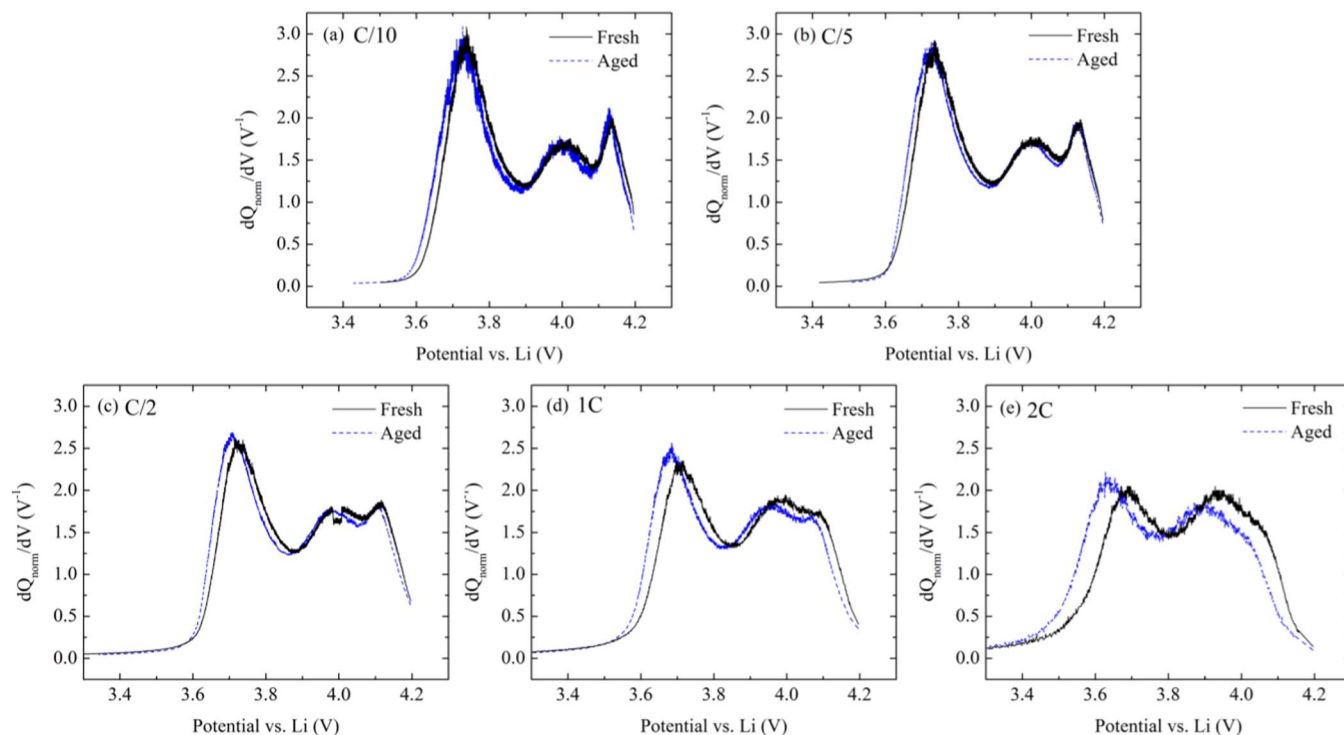


Figure 8. Differential-capacity curves of fresh and aged cathodes obtained at a discharge rate of (a) C/10 (b) C/5 (c) C/2 (d) 1C and (e) 2C. The differential-capacity is normalized with respect to the C/10 discharge capacity.

loss in the pouch cell is the loss of the limited amount of Li^+ due to parasitic reactions rather than the degradation of the positive and negative electrodes due to, for example, breakage of active material particles, cracks at the porous electrode, damage of the conductive matrix or disconnection between electrode components. In addition to the loss of Li^+ , electrolyte reduction at the negative electrode and its oxidation on the positive electrode lead to the production of gaseous species which decreases the stack pressure in the pouch cell and can cause local dry-out and, therefore, isolation of active material particles in both the positive and negative electrodes from the ionic path through the electrolyte. Gas formation is particularly noticeable in pouch cells that have been stored at 100% SOC and 60°C for a long period. It should be noted that parasitic reactions change the composition of the electrolyte and so could alter its transport properties in the pouch cells stored at 60°C . This effect could not be measured in the half-cell experiments since only fresh electrolyte was used for the coin cell assembly.

The loss of cyclable Li^+ ion has been predominantly attributed to the formation and growth of the SEI layer on the surface of graphite particles during calendar aging.³² In general, the SEI is formed on the surface of active particles during the formation cycles and continues to grow during battery life by the decomposition of electrolyte and subsequent reaction with Li^+ . This loss of Li^+ is irreversible for the most part and only a small fraction is recovered at the positive electrode via side reactions that insert Li^+ into the delithiated active material (i.e., reversible capacity loss) as mentioned before. Moreover, SEI growth impedes the transfer of Li^+ ion to/from the surface of the active material and so decreases the power capability of the electrodes (increased electrode polarization in Figure 7) and hence the pouch cell as it ages (Figure 6).

Data from the galvanostatic discharge curves in Figure 7 have been re-plotted in Figure 9 to show the dependence of the potentials of the positive and negative electrodes vs. Li/Li^+ on discharge current. The data are recorded at 10% depth of continuous discharge for both fresh electrodes and those obtained from the pouch cell aged at 60°C and 100% SOC for 9 months. During the early stages of discharge, the losses due to diffusive transport within both the active material and electrolyte should be small and so the variation of the potentials shown in Figure 9 primarily reflects ohmic losses at the particle and electrode levels. Increases in the electrode resistances due to aging can be calculated from the slope of the deviation between the potentials of the fresh and aged electrodes ($\Phi_{\text{fresh}} - \Phi_{\text{aged}}$) plotted as a function of discharge current. The positive electrode resistance is estimated to be $\sim 35\%$ larger than that of the fresh electrode resistance (i.e., $R_{\text{fresh}} = (U_{\text{fresh}} - \Phi_{\text{fresh}})/I$ where U_{fresh} is the equilibrium potential of the electrode at 10% depth of discharge). The resistance of the negative electrode increases more significantly after aging and is found to be $\sim 84\%$ larger than that of the fresh negative electrode, i.e., the aged negative electrode experiences almost twice as much polarization as the fresh one. Transport and kinetic limitations at the surface of active particles and ohmic losses across the electrodes are most likely responsible for the observed resistance increase in the aged electrodes.

Figure 10 shows SEM images of the surface of a fresh graphite electrode (Figures 10a–10d) and the surface of a graphite electrode aged at 100% SOC and 60°C for 9 months (Figures 10e–10h). The low magnification images of the aged sample clearly show the presence of two different layers on the surface of the anode (i.e., interface between the anode and separator) that bury the graphite particles. These layers differ from the much thinner SEI layer that forms on the graphite particle surface.^{7,11,33} The back-scattered electron micrograph and EDX elemental analysis clearly identify the composition of these layers: i) bright porous regions in Figures 10a–10c (fresh electrode) and Figures 10e–10g (aged electrode) that are made up of Al_2O_3 remaining from the coating on the separator and ii) smooth layer visible in the secondary-electron micrograph (most notably in Figure 10g for the aged electrode compared with Figure 10c for the fresh electrode) and appearing on the dark regions in the back-scattered electron micrograph that is a secondary passivating layer rich in oxygen ($\sim 47\%$), fluorine ($\sim 10\%$) and phosphorous ($\sim 2\%$) and presumably com-

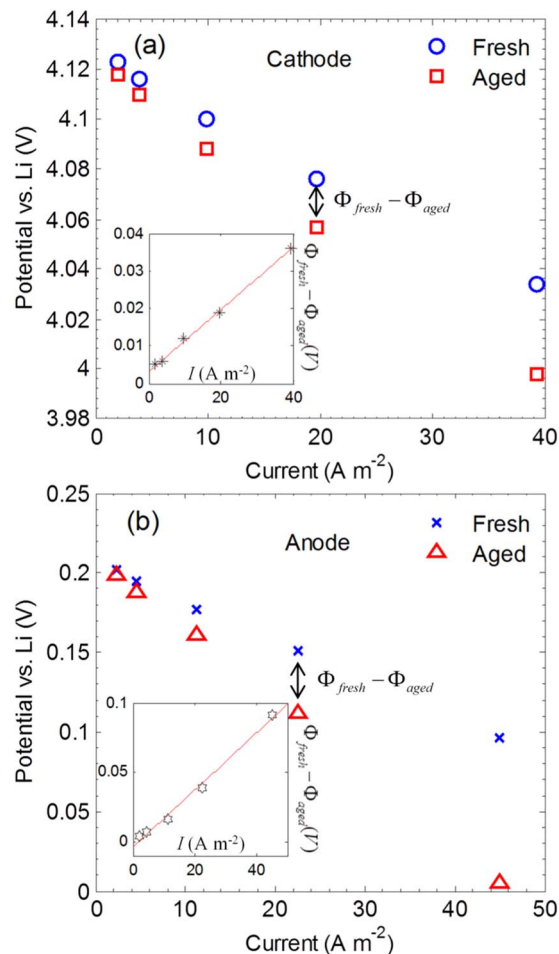


Figure 9. Variation of potential of (a) positive electrode and (b) negative electrode with discharge current recorded at 10% depth of discharge for fresh electrodes and those harvested from the pouch cell aged for 9 months at 60°C and 100% SOC storage condition. The insets show the increase of the polarization of the electrodes due to aging.

prise the organic and inorganic products of parasitic reactions. The formation of this secondary layer with an appreciable thickness and apparently low porosity (i.e., relative to the electrode itself) is expected to significantly contribute to the increase in the overall polarization of the aged anode as shown in Figure 9 and thus should be considered in aging models. These images show regions of the actual electrode that are not covered by the secondary layer. However, this is likely an artifact of the experimental procedure to dismantle the battery which leads to removal of portions of the layer with the separator. It should be noted that the separator adheres relatively strongly to both fresh and aged negative electrodes.

The surfaces of the graphite particles in the fresh and aged electrodes are compared at a higher magnification in Figures 10d and 10h. Although the differences in the surfaces of the fresh and aged anodes do not appear large in the images, the presence of an SEI layer in the aged sample is suggested in Figure 10h from the appearance of less sharply defined edges on the particles (due to low conductivity of SEI) and bright spots on the surface of graphite particles. EDX elemental analysis of the surface of the graphite particles in the aged negative electrode (Figure 10g) shows that it contains F and P with atomic percentages of $\sim 5.9\%$ and $\sim 0.8\%$, respectively, compared with only $\sim 0.9\%$ F and no detectable P in the fresh anode. Since F and P originate only from the solute in the electrolyte, this change in content reflects that some degradation of the electrolyte has taken place during aging. Also, a large increase in the O content is observed after aging ($\sim 21\%$) and is most likely related to the presence of oxygen-rich or-

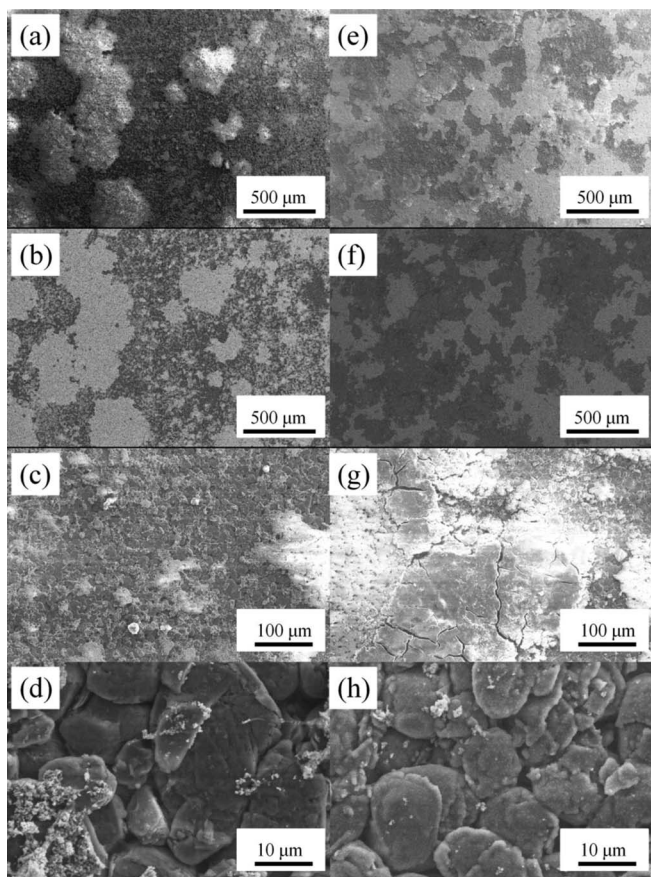


Figure 10. SEM image of the negative electrode surface in a (a)-(d) fresh electrode and (e)-(h) electrode aged at 100% SOC and 60°C for 9 months. (b) and (f) are back-scattered electron micrographs of the same areas shown in (a) and (e). (c) and (d) show regions in (a) and (g) and (h) show areas in (e) at higher magnifications.

ganic and inorganic compounds in the SEI layer such as lithium alkyl carbonates, Li_2CO_3 and Li_3PO_4 .

The SEM micrographs of the positive electrode show very little difference between the fresh and aged samples and so are not included here. EDX chemical analysis of the positive electrode, however, shows a significant increase in the F content in the aged sample. The F/Mn atomic ratio estimated for the LMO particles increases from $\sim 2.3\%$ in the fresh electrode to $\sim 14.7\%$ in the aged electrode, whereas the estimated F/NMC ratio for the NMC particles remains virtually the same in the fresh and aged electrodes. This observation suggests that the side reactions involving solute decomposition form an F-rich passivation layer primarily on the surface of the LMO rather than on the NMC particles. This is in line with the $\sim 35\%$ increase in the cathode total resistance in Figure 9a and more specifically the larger NMC/LMO peak intensity ratio in the differential-capacity curves of the aged cathode compared to the fresh one at high rates shown in Figure 8e.

The effects of contamination and reaction with O_2 and moisture during sample transfer to the microscope should not be ignored.³⁴ No trace of Mn, Ni and Co is found in the EDX elemental survey of the aged negative electrode surface. However, ICP analysis shows an increase in the concentration of Mn in the aged negative electrode ($\sim 175 \text{ mg kg}^{-1}$ anode) compared to the fresh one ($\sim 18 \text{ mg kg}^{-1}$ anode), consistent with previous reports.¹¹ On the other hand, virtually no change of the Ni and Co content in the negative electrode is observed after aging. The increase in the F/Mn ratio on the LMO particles as observed in the EDX analysis and the significant rise of the electrode resistance could be indicative of the concurrent Mn dissolution and formation of a poorly conductive passivation layer on the surface of the LMO

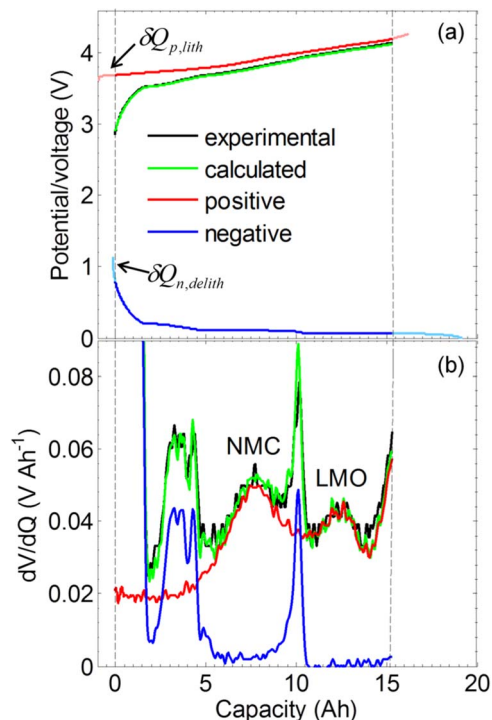


Figure 11. (a) Experimental voltage-capacity curve of a fresh cell compared with the calculated curve from differential-voltage analysis. (b) Comparison between experimental and calculated differential-voltage curves as a function of cell capacity.

particles which leads to a small deterioration of LMO and 2.7% capacity loss (at least partially) of the positive electrode measured by the half-cell experiments. A more detailed discussion of the formation and composition of the SEI layer can be found in Refs. 22,35–39.

Differential-voltage analysis.—As mentioned previously, gas buildup is very noticeable in pouch cells stored at 100% SOC and 60°C and is expected to affect the cell performance. Gas bubbles in pouch cells decrease the stack pressure leading to an increase in contact resistances and tend to isolate active particles from the ionic conduit by pushing electrolyte out of pores of both the positive and negative electrodes. The latter affects the electrode performance in two ways: i) apparent loss of active material due to blockage by gas bubbles and ii) decrease in the effective transport properties within the separator and two electrodes due to a reduction of the electrolyte-filled pore volume and increase in tortuosity of the ionic path. Both the loss of Li^+ inventory and gas buildup lead to the capacity fade of the pouch cells and should be addressed simultaneously. Although gas formation appears to be a major degradation mode, estimation of associated performance losses has not been reported to the best of our knowledge. In addition, the reduction in the operating stoichiometry windows of the positive and negative electrodes due to this degradation mode also has yet to be estimated. These aspects are analyzed quantitatively by means of the following differential-voltage analysis.^{40,41}

Differential-voltage analysis is used in order to quantify the contributions of the two degradation modes. By differentiating the cell voltage with respect to capacity (i.e., dV_{cell}/dQ vs. Q), this analysis transforms the features of the voltage-capacity curves into visible peaks (Figure 11) and enables more accurate assessment of the evolution of the voltage-capacity curves with aging time. To this end, the differential-voltage curve (black curve in Figure 11b) is estimated from the C/5 galvanostatic charge data (black curve in Figure 11a) of the cell at any storage time by subtracting the differential-potential curve of the negative electrode (i.e., $-dU_n/dQ$ vs. Q , blue curve in Figure 11b) from that of the positive electrode (i.e., dU_p/dQ vs. Q ,

red curve in Figure 11b) which have been obtained from half-cell charge/discharge experiments at $C/25$. Low C -rates are ideal for this analysis where the differential-voltage peaks are more clearly separated. The charge/discharge experiments on fresh cells have shown that the differential-voltage curve at $C/5$ almost perfectly matches the curve obtained at a rate as low as $C/25$ and so $C/5$ has been chosen as the lower bound of the applied currents during periodic cycling experiments for convenience. The calculated differential-voltage curve can then be compared with the actual experimental curve for the pouch cell. Most importantly, this analysis allows the contributions of the positive and negative electrodes to the cell differential-voltage curve to be estimated and their changes with time tracked. This procedure involves the adjustment of unknown parameters which reflect cell degradation so that the peaks of the calculated curve match those of the experimental ones.

The cell voltage V_{cell} corresponds to the difference between the positive electrode potential U_p and the negative electrode potential U_n :

$$V_{cell}(Q) = U_p(Q) - U_n(Q) \quad [1]$$

where Q is the cell capacity during the intermediate charge/discharge cycles conducted to characterize the change in the performance of the cells at 1-month intervals during storage (as described in the Experimental section) and is related to the Li fractions y_p and y_n in the fresh positive and negative electrodes, respectively, according to:

$$Q = \alpha_p A_p q_{p,max} (1 - y_p) - \delta Q_{p,lith} = \alpha_n A_n q_{n,max} y_n - \delta Q_{n,delith} \quad [2]$$

where A_p and A_n are the total areas and $q_{p,max}$ and $q_{n,max}$ are the maximum area-specific capacities of the positive and negative electrode, respectively. y_p and y_n vary between 0 for fully delithiated to 1 for fully lithiated electrodes. Eq. 2 is written for pouch cell charging so that $Q = 0$ marks the beginning of positive electrode delithiation and negative electrode lithiation. Due to factors such as the presence of gas bubbles, not all of the active material in each electrode is accessible to the Li^+ ions as described before. The terms α_p and α_n account for the mass fraction of the active material in the positive and negative electrodes, respectively, actually available for lithiation/delithiation. Since they effectively scale the electrodes down to smaller sizes, we refer to α_p and α_n as scaling factors. The terms $\delta Q_{p,lith}$ and $\delta Q_{n,delith}$ account for the loss of cyclable Li inventory. $\delta Q_{p,lith}$ represents the deviation in the maximum lithium content of the positive electrode achievable in the pouch cell at any time during storage relative to that in the fully lithiated electrode achievable in the half-cell experiments (i.e., not limited by the amount of Li^+ in the cell). Similarly, $\delta Q_{n,delith}$ represents the deviation of the minimum Li content of the negative electrode achievable in the pouch cell from the completely delithiated state. Thus, for given scaling factors, $\delta Q_{p,lith}$ and $\delta Q_{n,delith}$ determine the upper and lower bounds, respectively, of the operating stoichiometry windows of the positive and negative electrodes. To summarize, Eq. 2 gives an expression for the cell capacity Q that varies during intermediate charge/discharge cycles between $Q = 0$ at the beginning of charge and $Q = Q_{max}$ at the end of charge. However, the range of operation decreases during storage because Q_{max} drops due to gas generation and loss of cyclable Li manifested in the shift and contraction of U_p and U_n curves, which are accounted for in Eq. 2 by the parameters α_p , α_n , $\delta Q_{p,lith}$ and $\delta Q_{n,delith}$.

As shown in Figure 5a, a negligible amount of degradation occurs during the intermediate characterization cycling tests. Therefore, the terms α_p , α_n , $\delta Q_{p,lith}$ and $\delta Q_{n,delith}$ can be assumed to vary only with storage time and remain constant throughout the intermediate tests (i.e., ~3 days at room temperature). Thus, our main concern in this analysis is battery aging during storage and not during the intermediate characterization tests.

The differential-voltage of the cell during the intermediate charging steps is obtained by differentiating Eq. 1 with respect to Q and making use of Eq. 2 to yield:

$$\frac{dV_{cell}}{dQ} = \frac{1}{\alpha_p A_p q_{p,max}} \frac{dU_p}{d(1 - y_p)} - \frac{1}{\alpha_n A_n q_{n,max}} \frac{dU_n}{dy_n} \quad [3]$$

where the terms α_p , α_n , $\delta Q_{p,lith}$ and $\delta Q_{n,delith}$ are taken to be constant when differentiating Eq. 1 with respect to Q . The differential-voltage curves calculated according to Eqs. 1–3 are fitted to the experimental ones by adjusting α_p , α_n , $\delta Q_{p,lith}$ and $\delta Q_{n,delith}$. In doing so, we assume that the gas bubbles decrease the active area of the two electrodes to the same extent, implying that α_n and α_p are proportional to each other. Although gaseous species are formed and consumed at the positive and negative electrodes at different rates, it is not possible with the available information to measure the contribution of each electrode to the gas content of the cell. It is likely that gas evolves from each electrode and disperses throughout the cell and on average affects the performance of the two electrodes to the same extent. As will be shown, the results of the curve fitting appear to confirm this assumption.

The pouch cells used in this study consist of 17 negative and 16 positive double-side coated sheets. The negative electrode sheets are slightly larger (19.2 cm × 14.5 cm) than the positive electrode sheets (18.9 cm × 14.15 cm) (i.e., $A_p/A_n \cong 0.96$) to avoid Li plating at their edges. The outward facing sides of the negative sheets at the two ends of the stack are practically inaccessible and so not included in the calculations. The capacity available at the overhang of the negative electrode is assumed to be unused and so the ratio α_n/α_p is constrained in the fitting procedure to be ~0.96–0.98.

The result of the differential-voltage analysis applied to the charge of a fresh cell is demonstrated in Figure 11. As shown in Figure 11b, the calculated differential-voltage curve matches the experimental data very well. Also, the characteristic peaks for LMO, NMC and graphite are clearly identified. We obtain this fit by manually adjusting $\delta Q_{p,lith}$ and $\delta Q_{n,delith}$ while setting $\alpha_p = 1$, under the assumption that no gas is present in a fresh cell. As will be shown, the value of $\delta Q_{n,delith}$ remains unchanged whereas $\delta Q_{p,lith}$, α_p and α_n change and reflect losses in cell capacity during degradation. The fitting procedure is helped by knowing that $\delta Q_{p,lith}$ is sensitive to leftward shifts in the peak positions in the differential-voltage curve for the positive electrode, while α_p is sensitive to the separation between the NMC and LMO peaks for the positive electrode and α_n to the separation between the two main graphite peaks for the negative electrode.

Figures 12 and 13 show the results of the differential-voltage analyses during charge of the cells stored at a fully charged state at 35°C and 60°C, respectively, over the course of their aging periods. The differential-voltage characteristics of these cells are determined periodically as they age; in the case of the cell stored at 60°C, they are also measured after the low-rate discharge (Figures 13n) and the compression procedure (Figure 13o). In all cases shown in Figures 12 and 13, the agreement between the experimental and fitted curves is excellent. It can be seen in Figure 12 that both the shift in the peak positions and their separation evolve very slowly when the cell is stored at 35°C. Similar trends in the evolution of the differential-capacity curve with storage time are observed for the cell stored at 60°C, but the changes occur at a much faster rate, as evident in Figure 13. It turns out that the assumption of constant α_n/α_p is reasonable for both storage temperatures as the separation between the peaks for the negative electrode and between the peaks for the positive electrode vary proportionally to each other. The peaks in the experimental curves become less clearly defined as the cell ages due to progressively larger potential losses due to SEI growth and gas buildup. This is particularly visible in the data obtained from the cell aged at 60°C for longer than 4 months (Figures 13f–13m). Note that this analysis considers only the loss of cell Li inventory and loss of access to active particles due to gas buildup, but not that of polarization and mass transport. Consequently, it cannot account for the entire loss of the cell voltage due to aging.

The loss of cyclable Li inventory can be inferred from the difference in the values of $\delta Q_{p,lith}$ at different stages of aging and its value for the fresh cell. We have used this idea to examine the variation of cyclable Li loss with storage time for the cells stored at 100% SOC and 35°C and 60°C. Contrary to our expectations, the results presented in Figure 14 show that the loss of cyclable Li in the cells stored at 60°C is not much larger than that in the cells stored at 35°C.

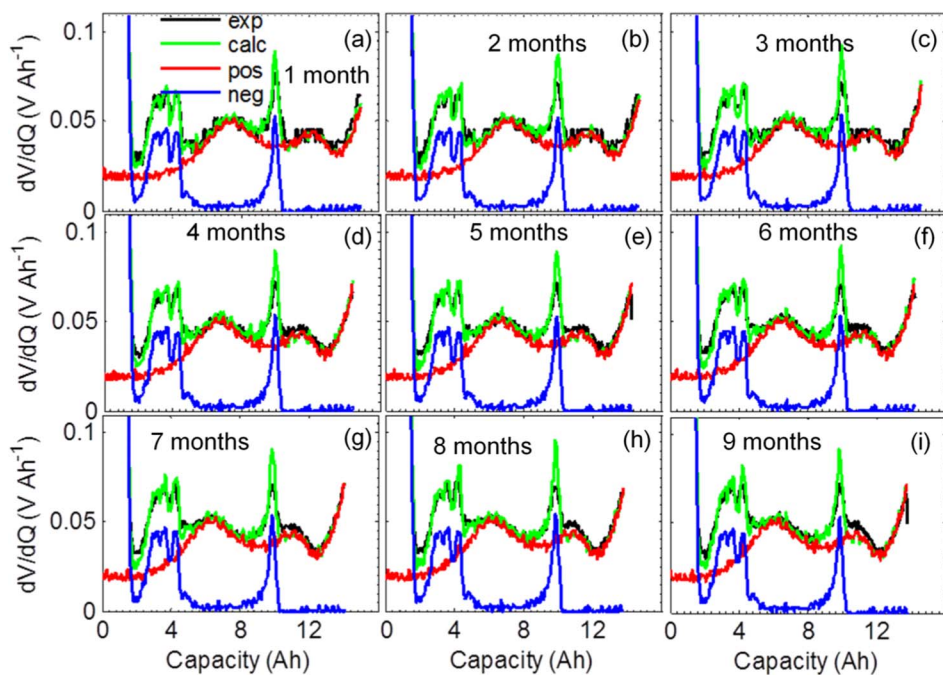


Figure 12. Comparison between experimental and calculated differential-voltage curves at different stages of aging for one of the cells stored at 35°C and 100% SOC.

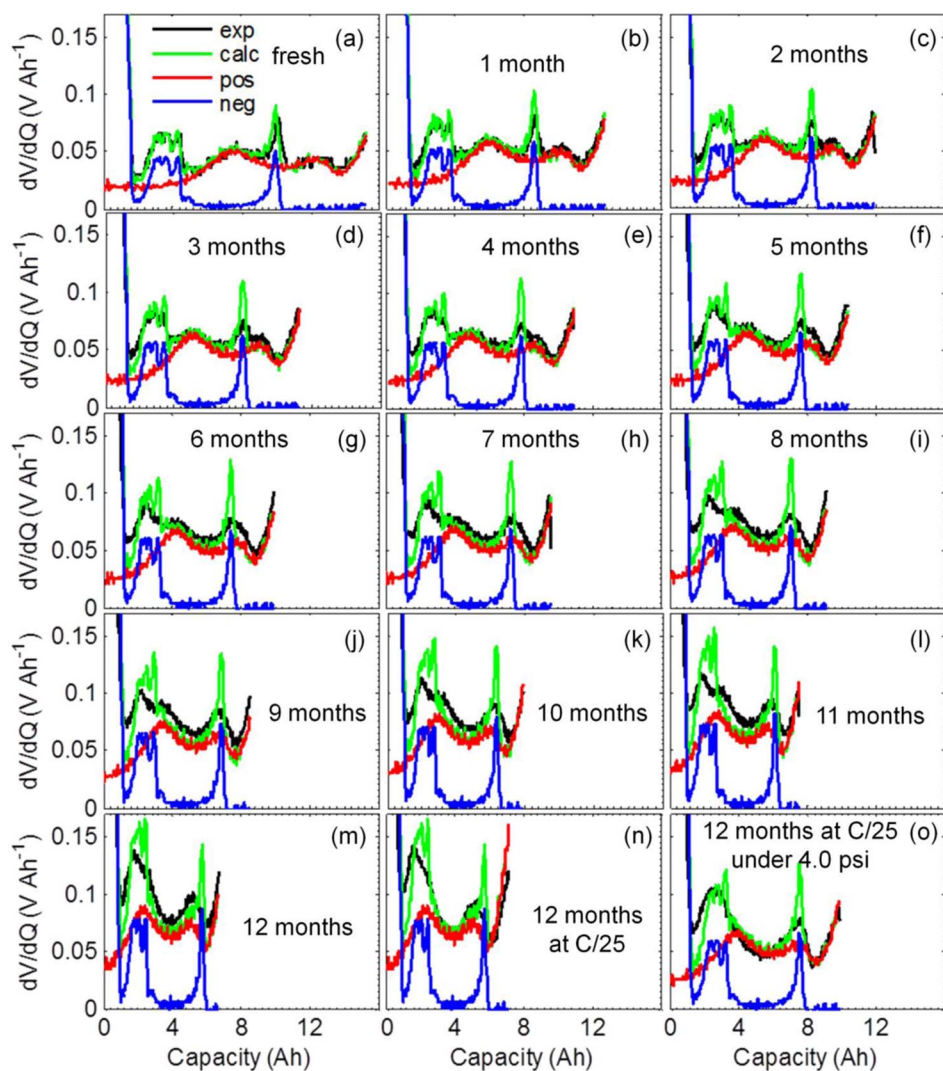


Figure 13. (a–m) Comparison between experimental and calculated differential-voltage curves at different stages of aging for one of the cells stored at 60°C and 100% SOC and after subsequent (n) low-rate charge and (o) compression procedure.

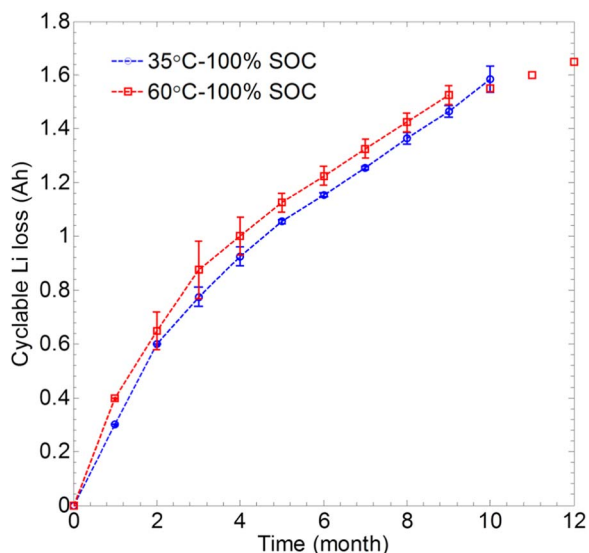


Figure 14. Loss of cyclable Li inventory as a function of storage time at 35°C and 60°C calculated from the differential-voltage analysis. No replicate is available for the last three data points at 60°C (square marker) since one cell was opened for post-mortem analysis after 9 months. Error bars are determined from the standard deviation of the mean values.

Figure 15 shows the evolution of the fraction $(1 - \alpha_p)$ of the electrode area covered by gas bubbles, also termed electrode dry-out, with aging time, as determined from the variation of the estimated α_p , assuming that the permanent loss of active material or active particle isolation is negligible. This assumption is supported by the post-mortem analysis presented in the previous sub-section, i.e., the maximum loss of active material is found to occur in the positive electrode, but is less than $\sim 2.7\%$ of the fresh electrode capacity. A sharp increase in the electrode dry-out is observed over the first month of storage at 60°C followed by a more gradual change thereafter until the end of the experiment. This trend is consistent with the overall drop in cell capacity shown in Figure 4. In contrast, very little gas is generated in the cells stored at 35°C and is reflected by the observation that the scaling factor α_p changes by only $\sim 2\%$. Interestingly, the

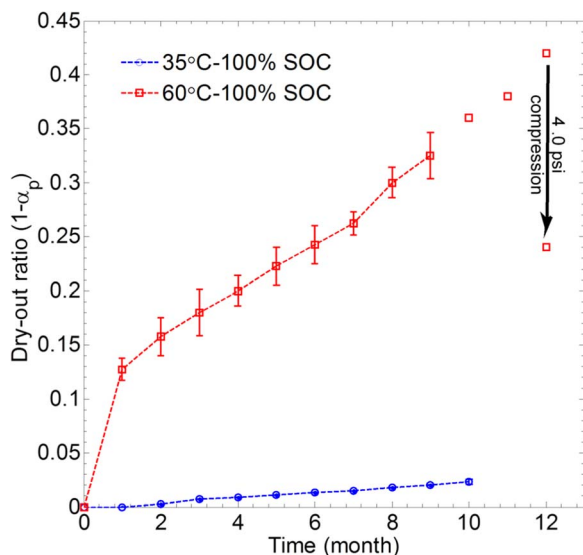


Figure 15. Evolution of electrode dry-out due to gas generation, as calculated from the differential-voltage analysis. The impact of cell compression on dry-out after 12 months of storage is indicated by the black arrow. Error bars are determined from the standard deviation of the mean values.

Table I. Minimum Li concentration in the electrodes and their standard deviations for the fully charged cells stored at 35°C and 60°C.

Temperature	35°C	60°C
$y_{p,min}$	0.03 ± 0.01	0.03 ± 0.01
$y_{n,min}$	0.01 ± 0.00	0.01 ± 0.00

pouch cell subjected to 12 months of storage at 60°C and then to a compression of 4.0 psi exhibits a significant drop in the dry-out ratio of its electrodes from ~ 0.42 to ~ 0.24 . The same trend is observed in Figure 4 showing an increase in the achievable capacity when the cell is compressed. Further analysis of the compression test is presented in the next sub-section.

The stoichiometry windows of the two electrodes (overall Li fraction in the case of the blended cathode) vary with aging and can be calculated from Eq. 2 once the aging parameters are estimated. The upper and lower bounds of the positive and negative electrodes stoichiometry windows can be calculated by setting $Q = 0$ (i.e., beginning of charge) and $Q = Q_{max}$ (i.e., end of charge) according to:

$$\begin{aligned}
 y_{p,max}(t) &= 1 - \frac{\delta Q_{p,lith}(t)}{\alpha_p(t) A_p q_{p,max}} \\
 y_{p,min}(t) &= y_{p,max}(t) - \frac{Q_{max}(t)}{\alpha_p(t) A_p q_{p,max}} \\
 y_{n,min}(t) &= \frac{\delta Q_{n,delith}(t)}{\alpha_n(t) A_n q_{n,max}} \\
 y_{n,max}(t) &= y_{n,min}(t) + \frac{Q_{max}(t)}{\alpha_n(t) A_n q_{n,max}} \quad [4]
 \end{aligned}$$

where $y_{p,max}(t)$, $y_{p,min}(t)$, $y_{n,max}(t)$ and $y_{n,min}(t)$ are the maximum and minimum Li fractions in the positive and negative electrodes, while $Q_{max}(t)$ is the cell capacity at the end of the intermediate charges at any storage time t . The terms $\alpha_p(t) A_p q_{p,max}$ and $\alpha_n(t) A_n q_{n,max}$ in the denominators of Eq. 4 represent the portions of active material in the positive and negative electrodes, respectively, accessible for lithiation/delithiation for which the Li contents change (i.e., $\delta Q_{p,lith}(t)$ and $\delta Q_{n,delith}(t)$) due to side reactions and subsequent SEI growth. The designated upper and lower cutoff potentials of the electrodes determine the lower and upper bounds of their stoichiometry windows, respectively. For these estimates, the charge and discharge data for the positive and negative electrodes are obtained from half-cell experiments where the electrodes operate between 0.005 and 1.5 V vs. Li/Li⁺ and between 3.0 and 4.25 V vs. Li/Li⁺, respectively. For each electrode, the lower potential bound corresponds to the fully lithiated (i.e., $y_{p,max} = 1$ and $y_{n,max} = 1$) and the upper bound to the fully delithiated states ($y_{p,min} = 0$ and $y_{n,min} = 0$). It should be emphasized that electrodes in a pouch cell never reach their fully lithiated states even at $t = 0$ due to cell balancing and Li losses during the formation cycles. The decrease in $y_{p,max}$ and $y_{n,max}$ over the duration of storage is shown in Figures 16a and 16b, respectively. On the other hand, $y_{p,min}$ and $y_{n,min}$ remain virtually constant throughout cell storage, as shown in Table I. This occurs because the positive electrode reaches an almost fully delithiated state at the end of cell charge, while the negative electrode is almost fully delithiated at the beginning of charge.

As shown in Figures 16a and 16b, the storage temperature has a large effect on the stoichiometry windows of the electrodes and the rate at which they narrow with aging time. Despite small differences in the loss of cyclable Li in the cells when aged at 35°C and 60°C, the stoichiometry windows of the electrodes narrow much more significantly in the cells aged at the higher temperature. The dramatic electrode dry-out due to gas generation at 60°C causes the side reactions to occur only over a fraction of the battery active material that is wetted by the electrolyte. As a result, the loss of Li due to parasitic

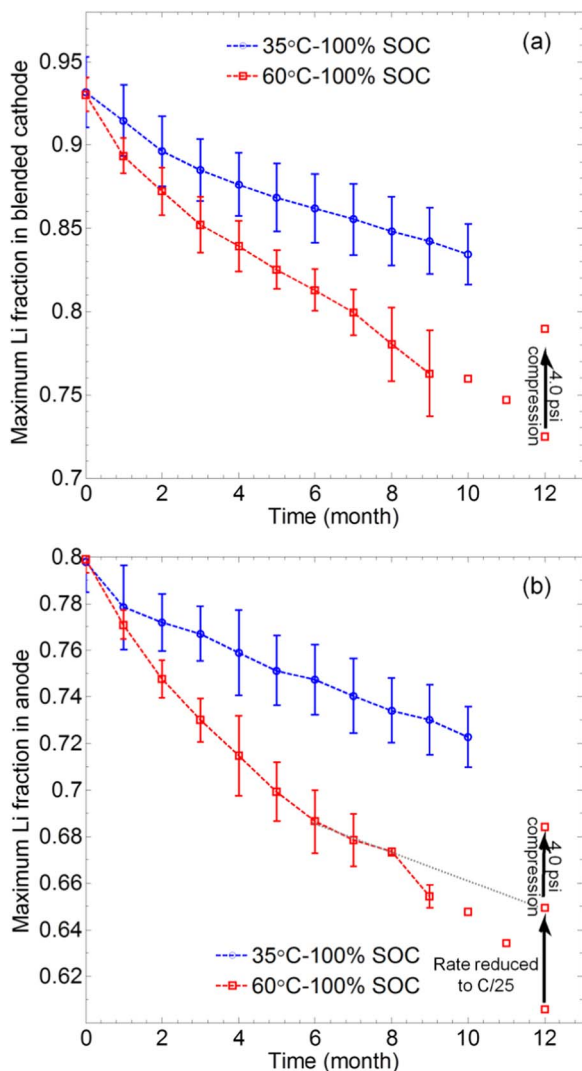


Figure 16. Maximum Li fraction in the (a) blended positive electrode calculated by normalizing maximum electrode capacity with respect to the total cathode capacity operating within 3.0–4.25 V (vs. Li/Li^+) potential window and (b) negative electrode calculated by normalizing maximum electrode capacity with respect to the total anode capacity operating within 0.005–1.5 V (vs. Li/Li^+) potential window. The impact of cell compression on capacity after 12 months of storage is indicated by the black arrow in the graph. Error bars are determined from the standard deviation of the mean values.

reactions affects the Li content in the wetted portions and should be normalized with respect to the accessible capacity which continuously decreases due to gas formation during aging (Eq. 4). Consequently, the calculated stoichiometry windows correspond only to the wetted active material particles. Mechanical compression decreases the dry-out ratio of the cell aged for 12 months at 60°C by a factor of two and thus increases the maximum Li fraction in the blended cathode from ~ 0.72 to ~ 0.79 and that of the negative electrode from ~ 0.65 to ~ 0.68 .

Effect of pressure.—When a commercial pouch cell is first manufactured, the space inside is filled with electrolyte. The cell is then sealed and undergoes formation cycles. The gas that accumulates during these formation cycles is removed and the cell re-sealed. Once the storage period begins, gas bubbles begin to appear particularly in the pouch cells stored at 60°C and 100% SOC. The gas buildup gradually increases while the cell is aging, as already discussed, causing the package surface to wrinkle when held between the fingers. Based on previous research, the gas most likely includes CO_2 , CO , C_2H_4 and

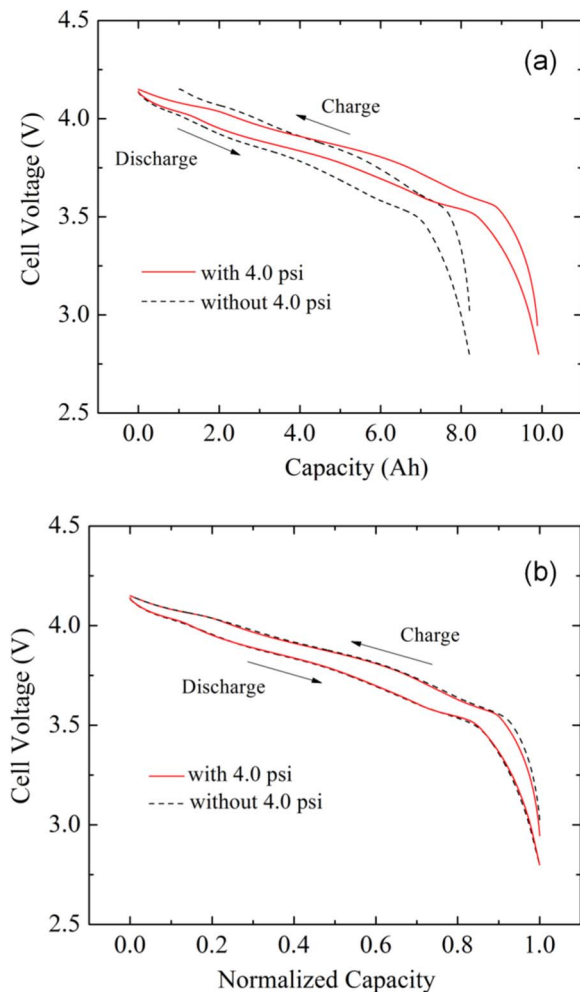


Figure 17. Comparison of cell voltage versus (a) capacity and (b) normalized capacity curves obtained at the rate of C/25 with and without the application of 4.0 psi pressure on the pouch cell aged during storage at 60°C and 100% SOC for 12 months.

C_2H_6 which are the products of side reactions at the two electrodes involving the electrolyte and active materials and/or impurities.

In order to investigate the effect of compression on the performance of the cells, we have conducted non-destructive tests involving force-loading of pouch cells aged at 60°C and 100% SOC for 12 months according to the procedure described in the Experimental section. On the basis of charge and discharge curves obtained at C/25, the capacity is found to increase from ~ 8.26 Ah when no pressure is applied to ~ 9.92 Ah when a 4.0 psi compression is applied (Figure 17a). However, a similar increase in pressure from 0 to 4.0 psi has virtually no effect on the potential-capacity curves when a fresh cell is tested (not shown). This difference indicates that the benefit of compression arises predominantly due to its effect on the gas generated during aging. According to our analysis, the large capacity gain of the aged pouch cells upon compression occurs in two ways: i) decrease in the cell dry-out ratio (Figure 15) and ii) widening of the available SOC windows or stoichiometries of both the positive and negative electrodes (Figures 16a and 16b) with the former having the main contribution to the capacity increase. When the capacity is normalized with respect to the maximum attainable capacity of the cell under each condition (i.e., the normalized capacity reaches 1.0 at the end of charge and discharge in each case), the two pairs of charge/discharge curves obtained with and without the applied pressure are found to overlap almost perfectly (Figures 17b). This demonstrates that the shapes of the charge/discharge curves are fairly similar with and without

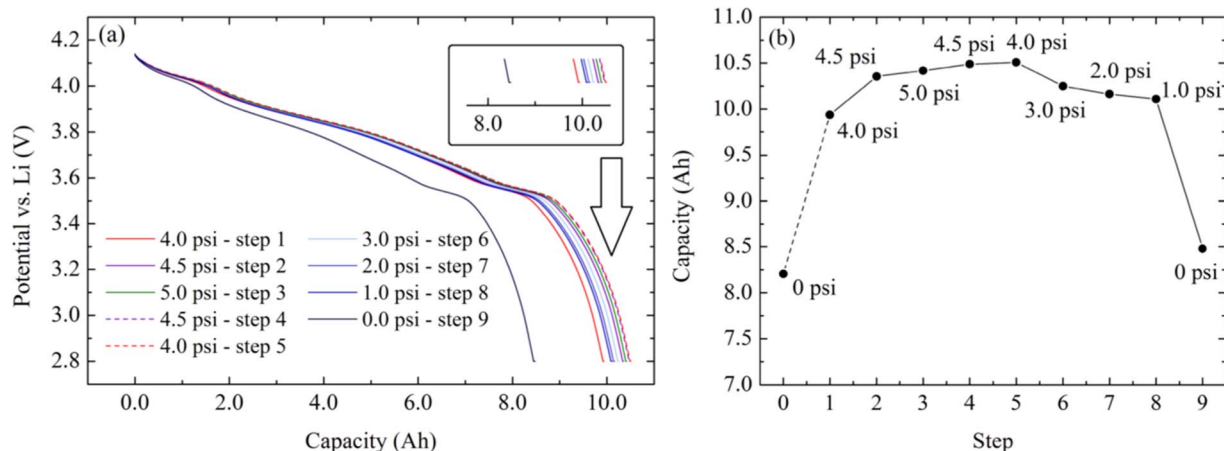


Figure 18. (a) Discharge potential-capacity curves and (b) capacity at the end of discharge measured at C/25 at each pressure applied in the sequence of 9 steps on the pouch cell aged during storage at 60°C and 100% SOC for 12 months.

compression and supports the conclusion that the improvement of capacity under force loading can be attributed primarily to the increase in the amount of active material effectively connected to the ionic path provided by the electrolyte.

The dry-out ratio estimated from the differential-voltage analysis (red curve in Figure 15) decreases by almost a factor of 2 from ~ 0.42 with no compression to ~ 0.24 when 4.0 psi pressure is applied, reflecting an increase in the accessible active materials in both electrodes. It should be noted that the differential-voltage analysis for the compressed cell is carried out using data from step 5 of the compression test described later (Figure 18) where the maximum capacity is achieved.

As described in the Experimental section, we also conducted an experiment in which the pressure was adjusted in 9 steps and the discharge capacity at C/25 was measured after each step. A comparison of the potential-capacity curves and the capacity at the end of discharge measured at each pressure are presented in Figures 18a and 18b, respectively. When the load is first increased from 0 to 4.0 psi, the measured capacity of the pouch cell jumps from ~ 8.26 Ah to ~ 9.92 Ah. The capacity increases more gradually to ~ 10.5 Ah as the

pressure is increased incrementally over the subsequent 2 steps and remains almost the same during steps 4 and 5 before dropping over the next 3 steps as the pressure is reduced to 1.0 psi. In the last stage, the compression is removed and capacity drops significantly. In fact, the measured capacity returns to its original value of 8.2–8.5 Ah at the end of the experiment when pressure is no longer applied, which is the state at the beginning of the experiment. Thus, we conclude that the compression test causes virtually no permanent change in the cell and electrode microstructure. Moreover, this experiment shows that a large fraction of cell capacity can be recovered by the application of mechanical compression as small as 1.0 psi.

The effect of pressure is depicted in the schematic diagram of the cross-section of an aged pouch cell in Figure 19. Figure 19a corresponds to the situation when no pressure is applied and shows gas bubbles distributed throughout the cell, including the separators and electrodes, interfaces between electrodes and separators and between the electrodes stack and the pouch bag. Gas bubbles can block some of the connections, e.g., electrolyte/active material interfaces, and cause the resistance to ionic transfer to rise, utilization of active materials to decrease and the pouch cell capacity to be lowered. The application of

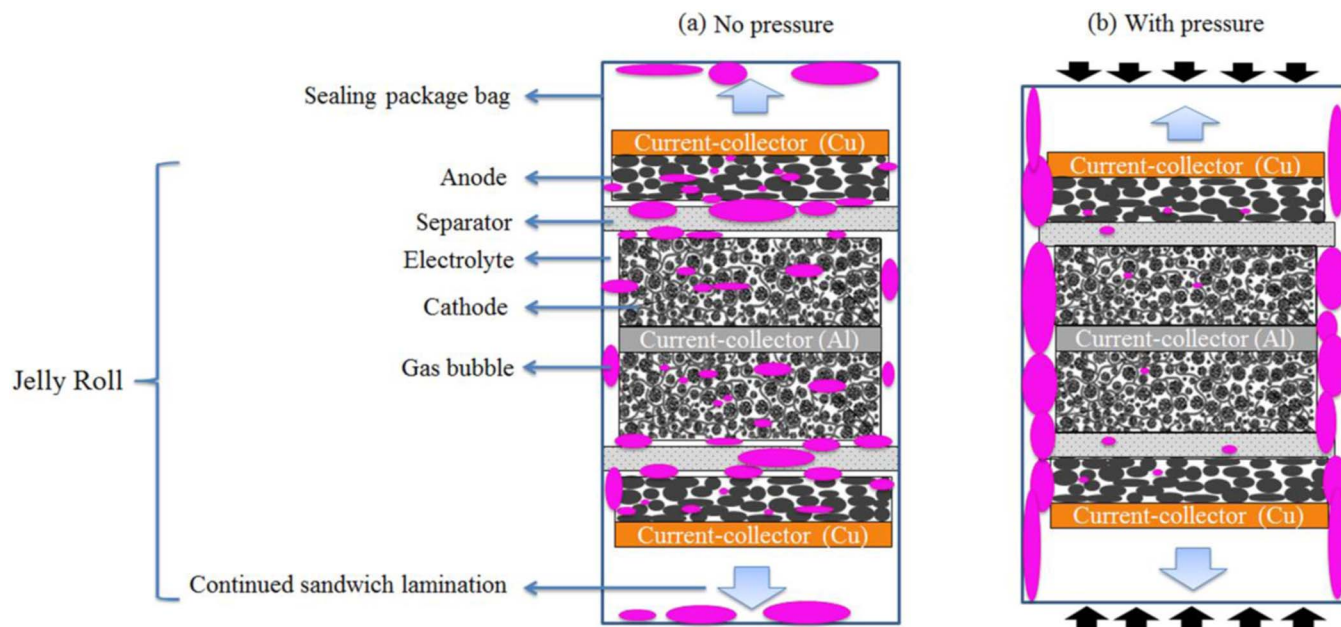


Figure 19. Schematic diagram of the cross-section of the aged pouch cell (a) without force-loading and (b) with force-loading.

even a small pressure should be sufficient to force most gas bubbles inside the cell out into the outer region at the interface between the stack and pouch bag where they have little effect on the operation of the cell (Figure 19b). Compression is also expected to enhance the physical contact between the various cell components that have deteriorated by aging (e.g., formation of a thick passivation layer on top of the negative electrode). However, contact resistance is likely to be less influential than electrode dry-out caused by gas generation inside the cell. The significant effect that pressure is observed to have on the capacities in Figures 17 and 18 was measured at the end of constant-current-constant-voltage discharges when the current reaches $C/25$ with the voltage held at 2.8 V. However, the effect of contact resistance on the cell capacity and voltage should be very small at such a low current. Also, the data in Figure 18 show that no correlation exists between the cell capacity and applied pressure over the range of 1–5 psi. A stronger positive correlation between pressure and capacity would be expected if contact resistance is the main contributing factor. Finally, we observed no evidence of electrode debonding or delamination when the cells were examined after being dismantled.

Conclusions

In this work, the calendar life of a commercial pouch cell consisting of a NMC-LMO blended cathode and graphite anode have been investigated through a series of non-destructive galvanostatic cell cycling and differential-voltage analysis and destructive post-mortem characterization of battery electrodes. In addition, the effect of pressure on the performance of an aged pouch cell has been investigated. The calendar life of the cells has been assessed under the following four storage SOC and temperature conditions: 0% SOC at 35°C, 0% SOC at 60°C, 100% SOC at 35°C and 100% SOC at 60°C. The conditions at the lower storage temperature and SOC are considered to be moderate for the cells, while storage at the higher temperature and SOC are sufficient to dramatically accelerate the degradation of the cell capacity. Not surprisingly, the fully charged pouch cell stored at 60°C exhibits the most rapid degradation so that the capacity remaining after 9 months of storage drops to ~57% of its original level.

Differential-voltage analysis reveals that about 30% of the active materials in both electrodes of the pouch cells aged for 9 months at 60°C and 100% SOC lose access to the electrolyte due to gas formation (i.e., electrode dry-out). On the other hand, gas generation is negligible in the cells stored at 35°C and 100% SOC for the same period of time. About 10% capacity loss is attributed mainly to the loss of Li inventory in the case of fully charged cell storage both at 35°C and at 60°C.

Coin cell measurements indicate that the loss of active material in the positive electrode harvested from cells stored at 60°C and 100% SOC is only about 2.7%, which can be regarded as the third most significant degradation mode in the cells studied here. These experiments also show that the active material loss in the graphite negative electrode is negligible. The polarization of aged positive and negative electrodes increases by ~35% and ~84%, respectively, compared to the level in fresh electrodes. The growth of the SEI layer on the negative electrode particles and the development of a passivation layer on the positive electrode particles could be responsible for the significant increase in the electrode resistances. A secondary passivating layer composed mainly of C, O, F and P is also observed on the surface of the aged negative electrode which is expected to increase the electrode resistance in addition to the SEI layer.

The significant increase in the F/Mn ratio of LMO particles in the aged cathode detected by EDX chemical analysis and increase in the Mn content of the aged anode identified using ICP-OES analysis suggest that Mn dissolution from LMO particles is likely accompanied by the formation of a F-rich passivation layer on the surface of LMO particles. This is a likely cause of cathode active material loss and the impedance increase upon calendar aging.

The compression test on the aged pouch cell showed that a large increase in capacity can be achieved by loading a force on an aged cell. Presumably this loading changes the distribution of gas bubbles inside the pouch cell by squeezing the gas from locations where it can hinder lithiation/delithiation of active particles to outer regions where it has little effect on cell operation and performance. Differential-voltage analysis indicates that this loading improves the utilization of active material by ~15% compared with that in the uncompressed pouch cell.

It should be noted that some of the results and observations obtained in this study are specific to the particular battery studied. For example, some of the results would likely change in an electrolyte solution with different composition (i.e., solvents, salt and additives). As well, a different material synthesis process would lead to different impurities in the electrode materials and influence the dominant degradation mechanisms including gas formation in the cell. However, the method of analysis presented here is universal and is applicable to any battery.

Acknowledgment

The authors express their appreciation to the General Motors Co., Automotive Partnership Canada (Project APCPJ 395996-09) and the Natural Sciences and Engineering Research Council of Canada (NSERC Project RGPIN-170912) for their financial support to conduct this research.

References

- S. B. Chikkannanavar, D. M. Bernardi, and L. Liu, *J. Power Sources*, **248**, 91 (2014).
- S. Jung, *J. Power Sources*, **264**, 184 (2014).
- Z. Mao, M. Farkhondeh, M. Pritzker, M. Fowler, Z. Chen, and M. Safari, *J. Electrochem. Soc.*, **162**, A716 (2015).
- Z. Mao, M. Farkhondeh, M. Pritzker, M. Fowler, and Z. Chen, *J. Electrochem. Soc.*, **163**, A458 (2016).
- Z. Mao, M. Farkhondeh, M. Pritzker, M. Fowler, and Z. Chen, *J. Electrochem. Soc.*, **164**, A39 (2017).
- Z. Mao, M. Farkhondeh, M. Pritzker, M. Fowler, and Z. Chen, *Electrochimica Acta*, **222**, 1741 (2016).
- B. Stiaszny, J. C. Ziegler, E. E. Krauss, J. P. Schmidt, and E. Ivers-Tiffée, *J. Power Sources*, **251**, 439 (2014).
- J. Wang, J. Purewal, P. Liu, J. Hicks-Garner, S. Soukiazian, E. Sherman, A. Sorenson, L. Vu, H. Tataria, and M. W. Verbrugge, *J. Power Sources*, **269**, 937 (2014).
- T. Waldmann, M. Wilka, M. Kasper, M. Fleischhammer, and M. Wohlfahrt-Mehrens, *J. Power Sources*, **262**, 129 (2014).
- M. Dubarry, C. Truchot, B. Y. Liaw, K. Gering, S. Sazhin, D. Jamison, and C. Michelbacher, *J. Power Sources*, **196**, 10336 (2011).
- B. Stiaszny, J. C. Ziegler, E. E. Krauss, M. Zhang, J. P. Schmidt, and E. Ivers-Tiffée, *J. Power Sources*, **258**, 61 (2014).
- P. Roder, B. Stiaszny, J. C. Ziegler, N. Baba, P. Lagaly, and H. D. Wiemhofer, *J. Power Sources*, **268**, 315 (2014).
- D. A. Stevens, R. Y. Ying, Reza Fathi, J. N. Reimers, J. E. Harlow, and J. R. Dahn, *J. Electrochem. Soc.*, **161**(9), A1364 (2014).
- C. P. Aiken, J. Xia, D. Y. Wang, D. A. Stevens, S. Trussler, and J. R. Dahn, *J. Electrochem. Soc.*, **161**(10), A1548 (2014).
- C. P. Aiken, J. Self, R. Petibon, X. Xia, J. M. Paulsen, and J. R. Dahn, *J. Electrochem. Soc.*, **162**(4), A760 (2015).
- J. Xia, C. P. Aiken, L. Ma, G. Y. Kim, J. C. Burns, L. P. Chen, and J. R. Dahn, *J. Electrochem. Soc.*, **161**(6), A1149 (2014).
- J. Self, C. P. Aiken, R. Petibon, and J. R. Dahn, *J. Electrochem. Soc.*, **162**(6), A796 (2015).
- R. Petibon, J. Xia, J. C. Burns, and J. R. Dahn, *J. Electrochem. Soc.*, **161**(10), A1618 (2014).
- D. J. Xiong, L. D. Ellis, K. J. Nelson, T. Hynes, R. Petibon, and R. J. Dahn, *J. Electrochem. Soc.*, **163**(14), A3069 (2016).
- D. J. Xiong, L. D. Ellis, R. Petibon, T. Hynes, and J. R. Dahn, *J. Electrochem. Soc.*, **164**(2), A340 (2017).
- I. Belharouak, G. M. Koenig Jr., T. Tan, H. Yumoto, N. Ota, and K. Amine, *J. Electrochem. Soc.*, **159**(8), A1165 (2012).
- M. Broussely, P. H. Biensan, F. Bonhomme, P. H. Blanchard, S. Herreyre, K. Nechev, and R. J. Staniewicz, *J. Power Sources*, **146**, 90 (2005).
- D. J. Xiong, R. Petibon, M. Nie, L. Ma, J. Xia, and J. R. Dahn, *J. Electrochem. Soc.*, **163**(3), A546 (2016).
- Y. Kim, *J. Solid State Electrochem.*, **17**(7), 1961 (2013).
- B. Michalak, B. B. Berkes, H. Sommer, T. Bergfeldt, T. Brezinsinski, and J. Janek, *Anal. Chem.*, **88**(5), 2877 (2016).
- C. L. Campion, W. Li, and B. L.ucht, *J. Electrochem. Soc.*, **152**(12), A2327 (2005).
- S. Käbitz, J. B. Gerschler, M. Ecker, Y. Yurdagel, B. Emmermacher, D. André, T. Mitsch, and D. U. Sauer, *J. Power Sources*, **239**, 572 (2013).

28. J. Schmalstieg, S. Käbitz, M. Ecker, and D. U. Sauer, *J. Power Sources*, **257**, 325 (2014).
29. M. Lewerenz, J. Münnix, J. Schmalstieg, S. Käbitz, M. Knips, and D. U. Sauer, *J. Power Sources*, **345**, 254 (2017)
30. N. N. Sinha, A. J. Smith, J. C. Burns, G. Jain, K. W. Eberman, E. Scott, J. P. Gardner, and J. R. Dahn, *J. Electrochem. Soc.*, **158**(11), A1194 (2011).
31. J. Christensen and J. Newman, *J. Electrochem. Soc.*, **152**(4), A818 (2005).
32. T. Joshi, K. Eom, G. Yushin, and T. F. Fuller, *J. Electrochem. Soc.*, **161**(12), A1915 (2014).
33. V. A. Agubra, J. W. Fergus, R. Fu, and S. Y. Choe, *J. Power Sources*, **270**, 213 (2014).
34. S. J. An, J. Li, C. Daniel, D. Mohanty, S. Nagpure, and D. L. Wood, *L. Carbon*, **105**, 52 (2016).
35. V. Agubra and J. Fergus, *Materials*, **6**(4), 1310 (2013).
36. M. Broussely, S. Herreyre, P. Biensan, P. Kasztajna, K. Nechev, and R. J. Staniewicz, *J. Power Sources*, **97**, 13 (2001).
37. D. Aurbach, H. J. Ploehn, P. Ramadass, and R. E. White, *J. Electrochem. Soc.*, **151**, A456 (2004).
38. B. Markovsky, Y. Talyossef, G. Salitra, H. Kim, and S. J. Choi, *J. Power Sources*, **162**, 780 (2006).
39. M. Broussely, P. H. Biensan, F. Bonhomme, P. H. Blanchard, S. Herreyre, K. Nechev, and R. J. Staniewicz, *J. Power Sources*, **146**, 90 (2005).
40. A. J. Smith, H. M. Dahn, J. C. Burns, and J. R. Dahn, *J. Electrochem. Soc.*, **159**(6), A705 (2012).
41. J. P. Schmidt, H. Y. Tran, J. Richter, E. Ivers-Tiffée, and M. Wohlfahrt-Mehrens, *J. Power Sources*, **239**, 696 (2013).